ADVANCING EARTH AND SPACE SCIENCES

Geophysical Research Letters

RESEARCH LETTER
10.1029/2024GL114506

A New Lunar Crustal Thickness Model Constrained by Converted Seismic Waves Detected Beneath the Apollo Seismic Network

D. Kim[1], V. Lekić[2], M. A. Wieczorek[3], N. C. Schmerr[2], G. S. Collins[1], and M. P. Panning[4]

[1]Earth Science and Engineering, Imperial College London, London, UK, [2]Department of Geology, University of Maryland, College Park, MD, USA, [3]Institut de physique du globe de Paris, Université Paris Cité, CNRS, Paris, France, [4]Jet Propulsion Laboratory, California Institute of Technology, Pasadena, CA, USA

Key Points:

- Reanalysis of shallow moonquake and artificial impact data provides updated crustal thickness estimates beneath Apollo stations 12, 15, and 16
- Frequency-dependent polarization analysis isolates target phases even in the presence of strong scattering
- New seismic tie-points with explicit uncertainty quantification yield GRAIL-based 29–47 km lunar crustal thickness models

Supporting Information:

Supporting Information may be found in the online version of this article.

Correspondence to:

D. Kim,
doyeon.kim@imperial.ac.uk

Citation:

Kim, D., Lekić, V., Wieczorek, M. A., Schmerr, N. C., Collins, G. S., & Panning, M. P. (2025). A new lunar crustal thickness model constrained by converted seismic waves detected beneath the apollo seismic network. *Geophysical Research Letters*, *52*, e2024GL114506. https://doi.org/10.1029/2024GL114506

Received 8 JAN 2025
Accepted 17 JUN 2025

Author Contributions:

Conceptualization: D. Kim
Data curation: D. Kim
Formal analysis: D. Kim, M. A. Wieczorek, N. C. Schmerr
Methodology: D. Kim, V. Lekić, M. A. Wieczorek, N. C. Schmerr
Supervision: D. Kim
Validation: D. Kim, V. Lekić
Visualization: D. Kim
Writing – original draft: D. Kim
Writing – review & editing: D. Kim, V. Lekić, M. A. Wieczorek, N. C. Schmerr, G. S. Collins, M. P. Panning

Abstract

Analysis of conversions between compressional and shear waves is a workhorse method for constraining crustal and lithospheric structure on Earth; yet, such converted waves have not been unequivocally identified in seismic data from the largest events on the Moon, due to the highly scattered waveforms of shallow seismic events. We reanalyze the polarization attributes of waveforms recorded by the Apollo seismic network to identify signals with rectilinear particle motion below 1 Hz, arising from conversions across the crust-mantle boundary. Delay times of these converted waves are inverted to estimate crustal thickness and wavespeeds beneath the seismometers. Combined with gravimetric modeling, these new crustal thickness tie-points yield an updated lunar crustal model with an average thickness of 29–47 km. Unlike previous models, ours include explicit uncertainty estimates, offering critical context for future lunar missions, geophysical studies, and predicting 15–36 km crust at Schrödinger and 29–52 km at Artemis III sites.

Plain Language Summary

The Moon's crust holds key information about its formation, evolution, and surface processes. Using seismic data from the Apollo missions, we identified moonquake seismic signals arising from the boundary between the Moon's crust and mantle, allowing us to obtain new estimates of crustal thickness beneath the Apollo landing sites. These signals had previously been difficult to detect due to extensive scattering caused by the highly fractured and heterogeneous lunar crust. By integrating our seismic estimates with gravity and topography data, we developed an updated global map of the Moon's crustal thickness, revealing an average thickness of 29–47 km and providing uncertainty quantification not available in previous models. Our results provide vital insights into the Moon's interior structure and offer valuable guidance for future lunar exploration and sustainable human activities on the Moon.

1. Introduction

The interior structure of the Moon holds a unique archive of processes that shaped and modified the crusts of all terrestrial planets early in their evolution. Spatial variations in lunar crustal thickness and density provide insight into the bombardment history of the inner solar system (Neumann et al., 2015) and how large impacts have fractured (e.g., Wahl et al., 2020), exposed (e.g., Miljković et al., 2015; Moriarty et al., 2021), and redistributed crust and mantle materials (e.g., Wieczorek et al., 2006). Estimates of absolute crustal thickness and density further constrain bulk composition (Taylor & Wieczorek, 2014) and porosity, with implications for the Moon's thermochemical evolution and the thermal conditions that govern ice-bearing capacity (Paige et al., 2010). These parameters are also directly related to the depth of the post-accretional magma ocean and the efficiency of the primary crust differentiation. In addition, the lunar crust also preserves a record of surface disturbances—including cratering, landslides, and seismotectonic activity—which reflects potential geological hazards relevant to future exploration (e.g., Haviland et al., 2022). A comprehensive analysis of crustal properties is therefore crucial for understanding planetary processes, in-situ resource utilization, and hazard mitigation, all of which are vital for future exploration and sustainable human habitation.

Despite significant advancements in lunar exploration, our understanding of the Moon's interior structure remains incomplete, relying primarily on indirect, remote measurements from gravitational, magnetic, and electromagnetic fields (Binder, 1998; Kivelson et al., 1992; Nozette et al., 1994). In contrast to these remote sensing methods, seismology is uniquely suited to directly probe the Moon's inaccessible interior. The Apollo missions'

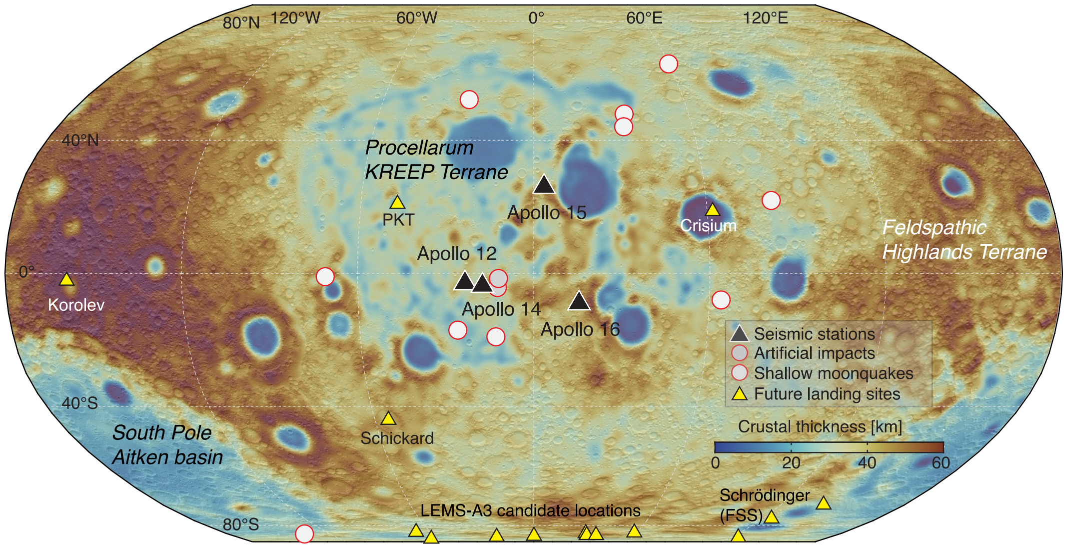

Figure 1. Global crustal thickness of the Moon. This model is constructed using new crustal thickness estimates beneath Apollo seismometers derived in this study as seismic tie-points for gravimetric modeling. The model assumes a crustal porosity of 12%, a mantle density of 3,220 kg/m^3, and uses a downward continuation filter with a half-amplitude at degree 80 (Supporting Information S1). The locations are plotted for shallow moonquakes (white) and artificial impacts (gray) with strong P- and S-wave polarization, as observed in this study. Event locations are from Bulow et al. (2005, 2007). Data are presented in a Robinson projection centered over the lunar nearside.

seismic experiments (Nakamura et al., 1982) revolutionized our understanding of the lunar crust. However, the inferred crustal properties—including composition, porosity, thickness, seismic wave speed, and their spatial variation—often seemingly contradict other geophysical and geochemical constraints (Khan et al., 2013; Lognonné et al., 2003). This is largely due to the geographic limitations of the seismic network, which was confined to the nearside of the Moon, and the limited fidelity and dynamic range of the recorded waveforms (e.g., Bulow et al., 2005). Consequently, crustal components from the existing seismic lunar interior models (Garcia et al., 2019) have limited global representation. Given the significant differences between the nearside and farside crusts, this limitation introduces bias into models of the Moon's interior and its dynamic processes.

Unlike Earth, where seismic analyses can take advantage of travel times and amplitude measurements of direct seismic waves, lunar seismograms are dominated by intense scattering in the regolith and megaregolith whose effects extend to longer wavelengths (Dainty et al., 1974). This scattering complicates the identification of conversions of compressional (P) to shear (S) waves—and vice versa—which is the workhorse technique for body-wave characterization of crustal thickness variations beneath seismic stations on Earth. The relative timing and amplitudes of these conversions, which are typically analyzed using the receiver function technique (Burdick & Langston, 1977), yields constraints on crustal thickness and wavespeed. Unfortunately, receiver functions are challenging to determine robustly in lunar studies (Shi et al., 2023); to date, only S-to-P conversions have been unequivocally detected in lunar data (Vinnik et al., 2001).

In this study, we reanalyze waveforms of shallow moonquake and artificial impact recordings initially considered at Apollo stations 11, 12, 14, 15, and 16, but retain only stations 12, 15, and 16 for detailed analysis based on data quality and event coverage (Figure 1). Building upon successful application of frequency-dependent polarization analysis (FDPA) to noisy InSight seismic data on Mars (Irving et al., 2023; Kim et al., 2022; Stähler et al., 2021), we apply this technique to search for P- and S-wave conversions and their multiples produced across the crust-mantle interface beneath each station. We highlight that our approach overcomes limitations of traditional receiver function analysis in the highly scattering lunar environment (e.g., Shi et al., 2023). After identifying crustal conversions, we measure their relative timing at Apollo 12, 15, and 16 and use these measurements to constrain crustal thickness, average seismic wavespeeds, and V_P/V_S ratios. Based on the newly derived thickness estimates at these seismic anchor points, we generate updated global maps of lunar crustal thickness by integrating GRAIL gravity (Zuber et al., 2014) and Lunar Reconnaissance Orbiter topography data (Smith, Zuber,

10.1029/2024GL114506

Neumann, et al., 2010), explicitly incorporating seismic uncertainties, which have not been accounted for in earlier models.

2. Data and Methods

2.1. The Apollo Shallow Seismic Events

The Apollo seismic network operated in (or adjacent to) the Procellarum KREEP Terrane (PKT) (Jolliff et al., 2000) on the Moon's nearside (Figure 1). We analyze the three-component seismic recordings from the Apollo Mid-Period sensors, focusing on all 28 shallow moonquakes and five artificial impacts of Saturn boosters and the lunar module on the Moon. Although the Apollo data set contains a greater number of deep moonquakes, we use shallow events due to their generally larger magnitudes, which yield larger signal-to-noise levels more suitable for identifying crustal converted waves. Raw seismic data from Apollo 12, 15, and 16 were resampled to 10 samples per second, and rotated to radial and transverse components based on existing lunar catalogs (Nunn et al., 2022) (Figure S1 in Supporting Information S1). Events with large ray parameters, which are insufficient for generating mode-converted waves at the crust-mantle boundary (e.g., Shi et al., 2023), were excluded based on the predictions using lunar internal structure model suites recently reassessed in Garcia et al. (2019). The very low seismic velocities of the lunar megaregolith imply that any seismic ray from the deep interior will reach the surface at near vertical incidence, yielding vertically polarized motions for P-waves and horizontally polarized motions for S-waves. We focus our analysis on a 30 s window before and after the P- and S-wave arrival times, within the 0.1–1 Hz frequency range, where the sensor is most sensitive. Most event recordings used for Apollo 12 and 16 were collected while the instruments were operating in peak mode (Lammlein et al., 1974). In contrast, the recordings from Apollo 15 were predominantly acquired during flat mode operation, with the exception of one event (Figure S1 in Supporting Information S1). Event data with notable glitches in the analysis window are discarded. Data from Apollo 11 and 14 were excluded due to their shorter operational duration and poor vertical-component quality, respectively (Nunn et al., 2020) (e.g., Figure S2 in Supporting Information S1).

2.2. Receiver Functions and Frequency-Dependent Polarization Analysis (FDPA)

Seismic waves traversing contrasts in wavespeed or density can convert between P- and S-waves, which can be detected and analyzed using the receiver function technique (Burdick & Langston, 1977). Receiver function analysis isolates these conversions by deconvolving the incoming seismic wave from the recorded waveform, allowing for the identification of subsurface boundaries, such as the crust-mantle interface, even from a single three-component seismic station (e.g., Kim et al., 2021). The first receiver function analysis using Apollo data set by Vinnik et al. (2001) identified precursory S-to-P converted signals preceding direct S-waves from stacked deep moonquake data at Apollo 12. Shi et al. (2023) attempted to estimate P-wave receiver functions from various lunar seismic events, but significant scattering in the seismic coda prevented them from achieving stable deconvolution. An alternative approach is polarization filtering, which can suppress scattered signals and enhance the detection of converted and reflected crustal phases. Goins et al. (1981) applied a time-domain polarization filter (Flinn, 1965) to deep moonquake data, investigating rectilinearly polarized signals following direct S-waves to infer the crustal structure beneath Apollo 16. Improving on earlier efforts, we apply a FDPA (Park et al., 1987) to shallow moonquake and artificial impact waveforms, filtering out scattered signals to identify crustal seismic phases.

Our polarization filtering process begins by computing the S-transform (Stockwell et al., 1996) of three-component waveforms and generating a 3×3 cross-spectral covariance matrix with 90% overlapping time windows, where window duration varies inversely with frequency. The eigenvalues of this covariance matrix represent the degree of polarization (DOP) (Koper & Hawley, 2010; Samson, 1983), while the eigenvectors describe the particle motion orientation in each time-frequency window. Complex components of the eigenvectors capture ellipsoidal particle motions, such as those associated with Rayleigh waves (Goodling et al., 2018). When one eigenvalue is much larger than the others, the corresponding DOP is high, and the complex-valued coefficients of the dominant eigenvector are in phase and the motion is rectilinear. We search for seismic arrivals with rectilinear particle motion, dominantly polarized in vertical (Vertical Rectilinear Motion: VRM) and horizontal (Horizontal Rectilinear Motion: HRM) directions, by combining polarization attributes derived from the FDPA:

10.1029/2024GL114506

$$\mathrm{VRM} = |\cos(\phi_{VH})| \times |\cos(\theta_v)| \times \mathrm{DOP} \tag{1}$$

$$\mathrm{HRM} = |\cos(\phi_{HH})| \times |\sin(\theta_v)| \times \mathrm{DOP} \tag{2}$$

where ϕ_{VH} is the phase angle difference between the vertical-horizontal components of the motion restricted to the range of $-90°$–$90°$; ϕ_{HH} is the phase angle difference between the two horizontal components, ranging from $-180°$ to $180°$; and θ_v is the vertical angle of incidence of the particle motion, bounded between 0° and 90° (Park et al., 1987) (see text in Supporting Information S1 for details). Because we restrict our attention to the HRM/VRM attributes extracted from the full FDPA, our results are not sensitive to the orientation of the horizontal components. Implementation of our FDPA has been successfully used to detect body and surface wave phases, such as ScS (Stähler et al., 2021), SKS (Irving et al., 2023), as well as minor-arc (Kim et al., 2022) to multi-orbit Rayleigh waves on Mars (Kim et al., 2023).

2.3. Implementation of FDPA to Individual Event Data and 3-D Synthetic Waveforms

Here, we apply our approach using P-wave data from a single seismic event on Mars, one shallow moonquake on the Moon recorded at Apollo 12, and 1-D synthetic lunar waveforms with added noise (Figure S3 in Supporting Information S1). Both the data and synthetic records show the expected P-wave particle motion, stronger in the VRM relative to the HRM (magenta, Figure S3 in Supporting Information S1). Following each P-wave arrival, strong HRM signals appear within a 10 s window (cyan, Figure S3 in Supporting Information S1), broadly consistent with predicted delay times for conversions at crustal interfaces. For Mars, we reference the velocity model from Knapmeyer-Endrun et al. (2021). For the Moon, our observations (∼7 s) are best matched by the average predictions across several lunar interior models (Figure S4 in Supporting Information S1), including M1 (∼7 s) and M3 (∼6 s) from Garcia et al. (2019), Weber et al. (2011) (∼8 s), and Garcia et al. (2011) (∼6 s), with the M2 from Garcia et al. (2019) predicting the shortest delay (∼5.6 s) (Figure S3 in Supporting Information S1). Notably, the back azimuth estimates for both this arrival and the direct P arrival are consistent with each other and align with the event's inferred back azimuth (inset, Figure S3B in Supporting Information S1). While polarization filtering is a non-linear process, and approaches like the S-transform or short-time Fourier transform impact the frequency window at which crustal phases are most clear, the average VRM and HRM envelopes across available frequencies and difference between the two are useful for identifying the presence and timing of specific target phases (Irving et al., 2023). Because individual results can be noisy due to incomplete noise removal and source effects not addressed by deconvolution, a complete analysis using multiple events is necessary for robust identification of the converted phases.

To validate our ability to extract P- and S-wave polarization attributes under strong crustal scattering on the Moon, we simulate 3-D wave propagation through crustal heterogeneities in order to generate highly-scattered waveforms typical of lunar records. These synthetic waveforms and their corresponding analyses are shown in Figures S5–S9 in Supporting Information S1. Details of the waveform generation and the input velocity models used in these simulations are provided in the text and Table S1 in Supporting Information S1. Using these 3-D synthetic waveforms, we demonstrate that the P-to-S conversion observed at ∼9 s—consistent with a crust-mantle boundary at 39 km depth in the hybrid model used in our 3-D scattering simulation—remains clearly detectable despite the presence of strong scattering. While polarization variability is observed across different scattering scenarios, we obtain robust results for both regional- (Figures S5–S9 in Supporting Information S1) and global-scale simulations (Figures S10–S11 in Supporting Information S1) when using a 750 m correlation length and 15% velocity and density heterogeneity (Korn, 1993; Saito et al., 2002)—parameters consistent with those inferred from the lunar crust for scattering envelope modeling of the SIVB impacts (Onodera et al., 2022) and other Apollo seismic data (Blanchette-Guertin et al., 2015). These results suggest that later-arriving scattered energy does not significantly influence the polarization attributes of earlier-arriving phases, further underscoring the robustness of our FDPA approach.

We apply this workflow to all shallow moonquake and artificial impact recordings at each seismic station (Figures S12–S17 in Supporting Information S1), measuring delay times and uncertainties for identified crustal phases (Figure 2). Given the relatively large uncertainties in the direct P- and S-wave arrival picks in Apollo data, we also reevaluated these picks by examining the corresponding VRM and HRM. If the polarization estimates did not match those predicted—VRM > HRM for P-waves and HRM > VRM for S-waves—or if no distinct arrivals were

10.1029/2024GL114506

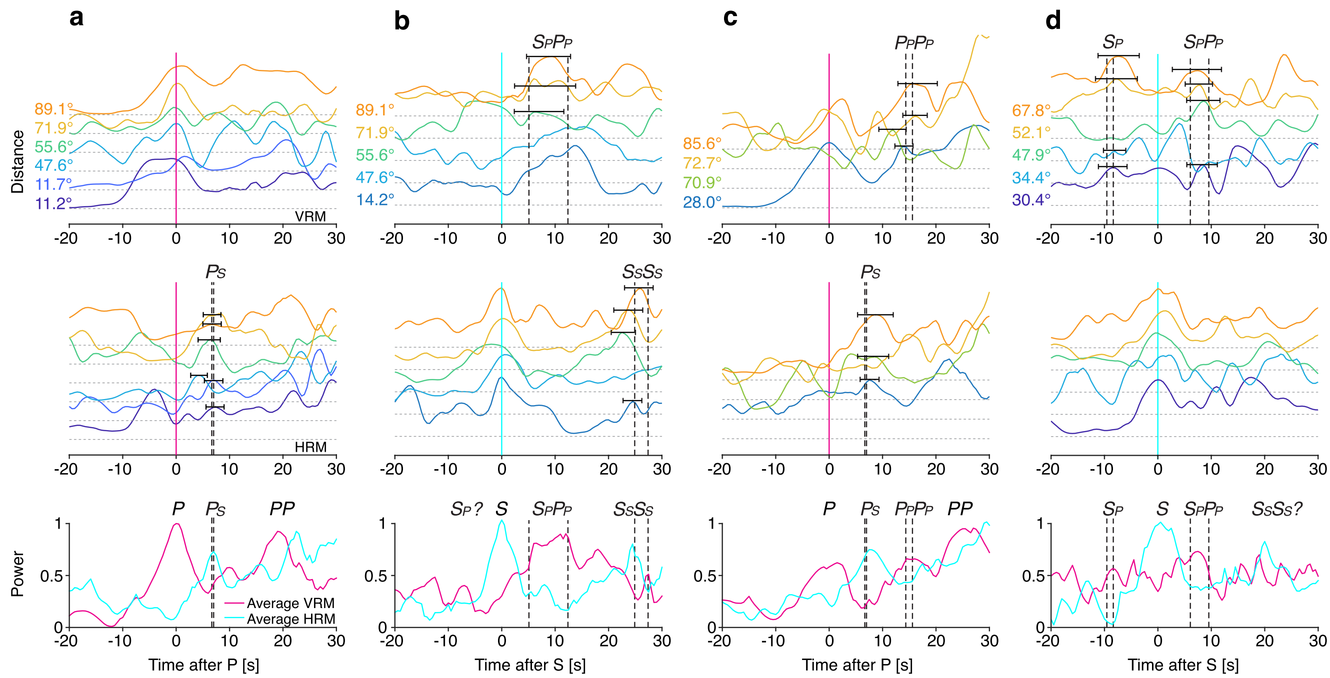

Figure 2. Frequency-dependent polarization analysis of Apollo seismic data. Analysis of vertical and horizontal rectilinear motions (VRM and HRM) for (a) P- and (b) S-waves from lunar events recorded at Apollo 12. Those events with strong polarization observed for the direct P-wave (magenta) and S-wave (cyan) are focused here (see main text). Event epicentral distances are indicated on the left of each polarization envelope. Dashed lines mark the predicted delay time range for various conversions based on all available lunar velocity models. Horizontal error bars represent 1-σ uncertainties used in the inversion. The bottom panel shows the average polarization power across analyzed events (c) Similar analysis for P-wave recordings at Apollo 16 and (d) S-wave recordings at 15. See Figure S18 in Supporting Information S1 for the bootstrap validation of the averaged VRM and HRM envelopes. Event origin times, in order of increasing epicentral distance, are: (a, b) 1972-12-10T20:22:23, 1971-07-29T20:50:23, 1975-02-13T21:55:23, 1973-06-20T20:15:21, 1976-03-06T10:06:11, 1971-04-17T06:54:09, 1973-03-13T07:51:09; (c) 1972-12-10T20:22:23, 1976-03-06T10:06:11, 1974-07-11T00:42:02, 1973-03-13T07:51:09; (d) 1976-01-14T11:10:12, 1976-03-06T10:06:11, 1976-03-08T14:34:16, 1975-01-12T03:07:04, 1975-11-10T07:46:08.

detected, we searched for alternative candidate arrivals within an 11 s window around the published P and S picks in the Apollo data (Nunn et al., 2020). Events without a clear signal within this window were excluded from the analysis (e.g., Figure S2 in Supporting Information S1). Ultimately, 12 events with clear indications of direct P- or S-wave polarization were retained (Figure S1 in Supporting Information S1). A systematic time adjustment was applied to the VRM and HRM envelopes to ensure the precise alignment of direct P-waves across all events with the maximum VRM and minimum HRM within the first 5 s window, and vice versa for direct S-waves. Finally, the aligned VRM and HRM envelopes were averaged across events at each station to produce stacked envelope, and the robustness of these stacks was assessed through bootstrapping (Figure S18 in Supporting Information S1).

3. Results

At $t = 0$ for P-waves, our average VRM envelopes for Apollo 12 and 16 show strong amplitude signals corresponding to direct P-arrivals (Figures 2a and 2c). For S-arrivals, HRM envelopes peak consistently across events analyzed at Apollo 12 (Figure 2b), while those at 16 are relatively less coherent, with multiple peaks and troughs within the P-coda window obscuring the S-arrivals (Figure S14 in Supporting Information S1). Despite significant scattering in the raw data, the observed dip and rise in the differential envelopes for P- and S-waves indicate the presence of rectilinearly polarized body waves from these events. At Apollo 15, this rectilinearity is less prominent (cf., VRM and HRM envelopes in Figures 2a–2d), which correlates with the generally lower signal-to-noise ratios apparent in the raw event recordings compared to Apollo 12 and 16 (Figure S1 in Supporting Information S1). This is consistent with expectations, as most recordings at Apollo 15 were made during flat mode operation, which could affect instrument stability (Nunn et al., 2020), and prior studies have noted significant amplification differences between vertical and horizontal components (Mark & Sutton, 1975), which could affect the resulting HRM/VRM.

10.1029/2024GL114506

Following the P-wave arrival, signals with horizontal rectilinear motion are consistently observed at lag times of 6–8 s for both Apollo 12 and 16. The timing and polarization of these signals indicate that these are direct Ps conversions at the crust-mantle boundary, which is present between 30 and 40 km depth, based on velocity models that favor a thinner lunar crust (Garcia et al., 2011; Lognonné et al., 2003; Weber et al., 2011). This depth is also compatible with the inferred depths from P- and S-wave travel time inversions (Chenet et al., 2006). We did not find evidence for the primary multiples or reflections of Ps phase, which would be expected at lag times of 10–20 s after the direct P-wave. Signals with more complex polarization at lag times of 20–30 s are likely associated with the PP phase, the free-surface multiple of the direct P-wave arrival, particularly for events with epicentral distance less than 65°. Unlike Apollo 12, Apollo 16 shows signals around 14 s, predominantly in the VRM envelopes (Figure 2c), likely corresponding to P-wave reflections off the crust-mantle boundary (PmP). The SS phase, which occurs beyond 30 s, falls outside the analysis window, and is not expected to affect these observations. Given the weak polarization of P-wave energy in Apollo 15 records, no significant arrivals are visible within the time intervals discussed (Figure S19 in Supporting Information S1).

On the S-wave records, coherent signals are observed at ~8 s and ~24 s in the S-coda at Apollo 12, corresponding to the expected timing of the primary multiple of the Sp phase (SpPp) and the crustal reflection of the direct S-wave (SmS). These signals were not observed at Apollo 16. Although a potential candidate for the 8 s arrival appears on the HRM envelopes at Apollo 16, the relative strength of VRM and HRM do not enable robust identification of multiples. Interestingly, similar SmS reflections at Apollo 16 were reported by Goins et al. (1981) in their analysis of deep moonquake records. With a presumably thicker crust beneath Apollo 16 (Chenet et al., 2006; Goins et al., 1981), two SmS phases in that study were identified at approximately 20 and 40 s, interpreted as S-wave reverberations between crustal interfaces at depths of 20 and 75 km, and the surface. Although the SpPp phase was not fully explored in their study due to its predicted small amplitude, small amplitude arrivals between the direct S- and SsPp (or SpSp) phases are visible in their best-quality waveforms. These arrivals could correspond to the SpPp phase, especially as the incoming waves approach the critical angle for events with small epicentral distances. At Apollo 15, possible indications of both Sp and SpPp arrivals are observed in the VRM envelopes. The precursor signals, observed ~8 s before the direct S-wave arrival, are consistent with the Sp phase previously identified by receiver function analysis of deep moonquakes at Apollo 12 (Vinnik et al., 2001), suggesting similar crustal thickness beneath Apollo 12 and 15. Furthermore, signals observed ~8 s after the direct S-wave arrival are interpreted as the SpPp phase, aligning well with predictions from available velocity models.

We quantify the relative delay time and uncertainties associated with those conversions and reflections for each event by the mean and standard deviation of a Gaussian fitted to the peak in the corresponding polarization envelope (VRM for waves with final leg P, HRM for S). Using these measurements, we infer seismic properties of the lunar crust, including crustal thickness, shear wavespeed (V_S), and compressional to shear wavespeed ratio (V_P/V_S) beneath each station using a grid search. This is analogous to the H-k-V stacking method often used on receiver functions in terrestrial records (Zhu & Kanamori, 2000). The prior ranges on the grid search are: 0–90 km for crustal thickness, 1–5 km/s for V_S, and 1.5–2.0 for the V_P/V_S ratio. To account for uncertainties in epicentral distance and moonquake depth, we also perturb these by ± 5° and 0–150 km, respectively, to estimate the ray parameter, which is needed when modeling delay times. Additionally, uncertainty in the lunar velocity model will contribute to uncertainty in the ray parameters; to account for this, we use three models from Garcia et al. (2019) that correspond to three different parameterization and inversion schemes developed by various authors (Drilleau et al., 2013; Garcia et al., 2011; Khan et al., 2014). From the χ^2 misfit between the measured delay times and predictions from the grid search, we compute the posterior joint probability distribution, obtaining the probability density function for each model parameter through marginalization.

We determine crustal thicknesses of 32.2 ± 6.7 km, 29.4 ± 6 km, and 41.1 ± 10.6 km (Figures 3a–3c; Table S2 in Supporting Information S1) and mean crustal V_S values of 2.6 ± 0.4 km/s, 2.2 ± 0.3 km/s, and 2.9 ± 0.6 km/s beneath Apollo 12, 15 and 16, respectively (Figure S20 in Supporting Information S1). Our thickness estimates for Apollo 12 and 16 are in good agreement with previous estimates based on GRAIL gravity data and Apollo seismic observations (Chenet et al., 2006; Wieczorek et al., 2013). This is partly expected, as the global thickness models used Apollo 12 crustal thickness as an anchoring seismic point, and our Apollo 12 thickness estimate falls between the values reported by Lognonné et al. (2003) (30 ± 2.5 km) and Khan and Mosegaard (2002) (35 ±

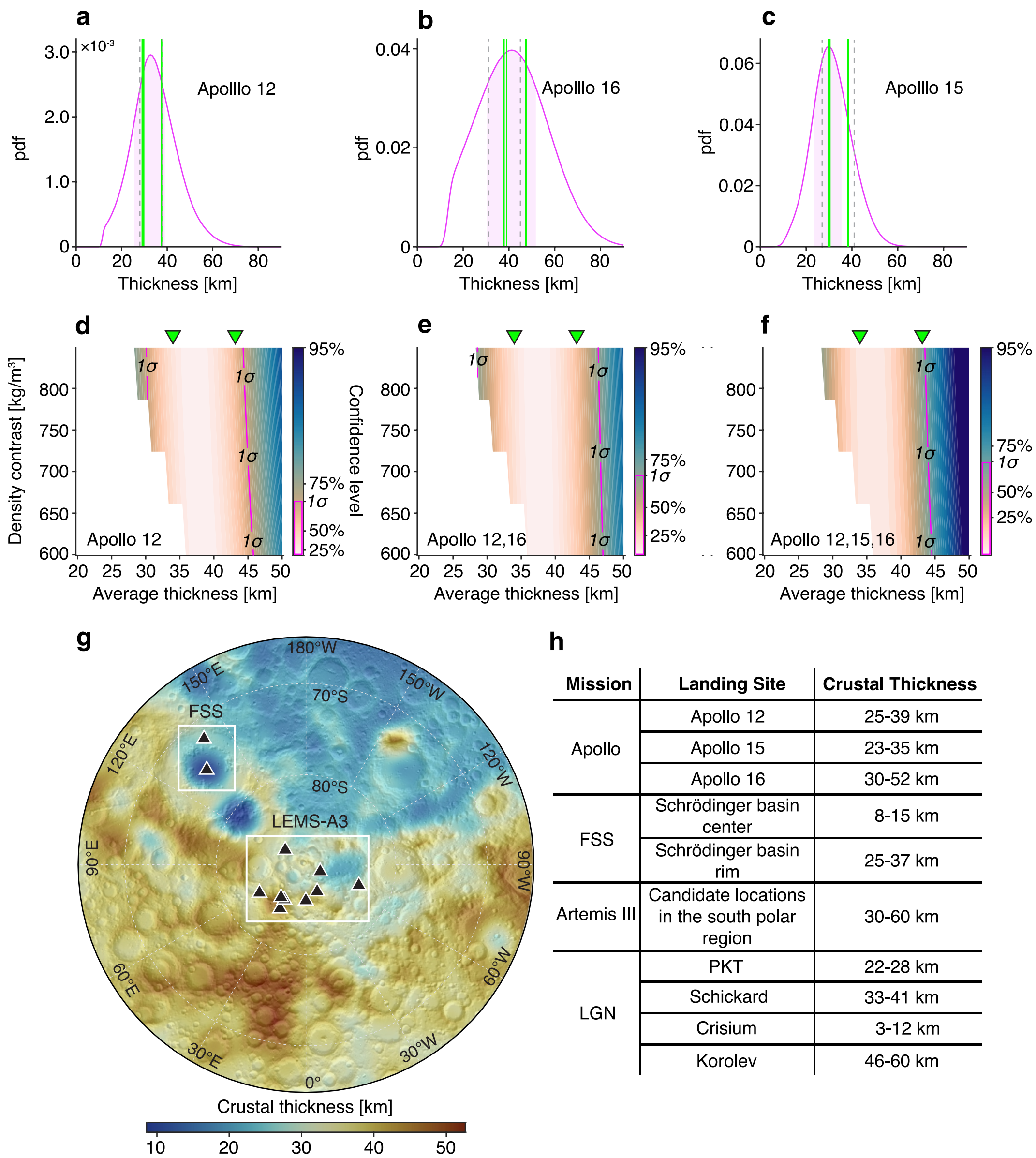

Mission	Landing Site	Crustal Thickness
Apollo	Apollo 12	25-39 km
	Apollo 15	23-35 km
	Apollo 16	30-52 km
FSS	Schrödinger basin center	8-15 km
	Schrödinger basin rim	25-37 km
Artemis III	Candidate locations in the south polar region	30-60 km
LGN	PKT	22-28 km
	Schickard	33-41 km
	Crisium	3-12 km
	Korolev	46-60 km

Figure 3. Crustal tie-points beneath the Apollo seismic network and global crustal thickness constraints. Posterior probability density functions (pdfs) for crustal thickness beneath (a) Apollo 12, (b) 16, and (c) 15. The green vertical lines mark the thickness estimates at each station from the previous GRAIL thickness map (Wieczorek et al., 2013). Gray dashed lines show crustal thickness estimates derived from P- and S-wave travel-time analysis by Chenet et al. (2006). See Figure S20 in Supporting Information S1 for the corresponding V_S and V_P/V_S ratio distributions. Confidence interval based on χ^2 misfit as a function of average crustal thickness and the density contrast between the crust and mantle, using crustal thickness estimates from (d) Apollo 12, (e) Apollo 12 and 16, and (f) Apollo 12, 15 and 16 as seismic tie-point(s) in the gravimetric modeling. Magenta contour line represents the 1-σ average crustal thickness range. The green triangles represent the two average crustal thickness estimates from previous GRAIL investigations (Wieczorek et al., 2013). All models consider a permissible crustal porosity range of 6%–12% and a mantle density range of 3,200–3,400 kg/m^3. (g) Updated global crustal thickness map from Figure 1 centered over the south pole, highlighting potential future landing sites (triangles). Unlike previous models, our map explicitly incorporates seismic uncertainty estimates. The map shown is for a crustal porosity of 12% and a mantle density of 3,220 kg/m^3. (h) Summary of crustal thickness estimates at Apollo seismometers and predicted thickness ranges beneath the landing sites of upcoming lunar missions.

5 km) (Table S2 in Supporting Information S1). Additionally, the V_S estimates are consistent with those from various existing interior models (Garcia et al., 2019), even though these were constructed with data with limited sensitivity to crustal wave speeds. In contrast, both the thickness and V_S at Apollo 15 are somewhat lower than

previous estimates (Figure 3c; Figure S20C in Supporting Information S1), which we attribute to the relatively poorer data quality and weaker polarization at this station. The V_P/V_S ratio remains poorly constrained, with mean values ranging from 1.8 to 1.9 across all stations (Figure S20 in Supporting Information S1).

To explore the trade-off between crustal thickness and seismic wavespeed, we conduct a sensitivity test by varying V_S within the interquartile range of the posterior distributions and examine changes in thickness variation across different stations (Figure S21 in Supporting Information S1). Our analysis of differences in crustal thickness between the stations indicates that the observed differences between Apollo 12 and 15, as well as between Apollo 12 and 16, are best explained when using the mean V_S for each station. Notably, the thickness difference between Apollo 12 and 16 spans a broad range, depending on the wavespeed combinations used. Similar V_S values are generally required to explain the GRAIL estimates at Apollo 12, 15, and 16 (Wieczorek et al., 2013), although a higher mean V_S at Apollo 16 is not strictly necessary to account for the observed difference. For Apollo 12 and 15, the difference is tighter, suggesting either similar thicknesses between the two or a slightly thicker crust at Apollo 12. The minimal difference observed in global crustal maps does not support a lower V_S at Apollo 12 relative to 15.

We interpret the observed converted or reflected seismic signals to originate from the crust-mantle boundary rather than shallow intracrustal interfaces. This is because even a 3 km thick megaregolith layer beneath the Apollo sites (Toksöz et al., 1974) cannot account for the >6 s delay times of the observed signals. Deeper intracrustal interfaces with sufficiently large wavespeed contrasts to produce P-to-S conversions might also be present. For example, mare volcanism, which has filled many impact basins across the PKT might produce such an interface, but a basaltic flow is unlikely to exceed 6 km even in the largest basins, and would be associated with a delay time of <2 s. At greater depths, sharp mantle discontinuities at approximately 100 km, potentially marking the transition between fractured and unfractured mantle materials (Gillet et al., 2017) would correspond to delay times greater than 20 s and therefore similarly cannot explain the observed signals.

The crustal structure beneath Apollo 12 has been the most thoroughly investigated, due to its longer seismic data coverage and higher-quality signals. Our thickness estimate and its uncertainty at Apollo 12 encompass previous estimates from other seismic studies, reanalysis of Apollo data, and published lunar interior models, suggesting that it is the most robust estimate for the crust-mantle boundary depth on the Moon. The thicker crust we find at Apollo 16, located in the Descartes highlands, is plausible given the region's higher topography and relatively lower bulk crustal density under Airy isostatic compensation (Wieczorek et al., 2013). The average V_S at Apollo 12 and 16 differs by 0.3 ± 0.7 km/s, implying that V_S at these sites is indistinguishable by our analysis. This is consistent with expectations based on petrological evidence because anorthosite and basalt are known to have only minor differences in seismic wavespeed (Chung, 1973). At Apollo 15, where we find the crust to be thinnest, the interpretation is more nuanced. The lower V_S and higher V_P/V_S ratio at Apollo 15 does not seem compatible with crustal compositions present beneath Apollo 12 and 16. Instead, they may indicate differences in other bulk crustal parameters, such as fracture density or porosity, or they may result from waveform complexity associated with internal interfaces. Since our analysis method does not eliminate source effects, however, we lack the resolution necessary to interpret detailed internal layering within the crust.

4. Global Crustal Thickness

The GRAIL crustal thickness models of Wieczorek et al. (2013) were anchored at Apollo 12 with crustal thicknesses based on two different types of seismic data (Table S2 in Supporting Information S1): reanalysis of the receiver function modeling from Apollo seismic records, which suggests a crustal thickness of 30 km beneath Apollo 12/14 (Lognonné et al., 2003), and P- and S-wave travel times, which indicate a slightly thicker crust of 38 km (Khan & Mosegaard, 2002). This resulted in two different global average crustal thicknesses being reported: 34 and 43 km. While capturing one aspect of seismic uncertainty, this approach does not account for the uncertainties inherent in the crustal thickness estimates derived from each type of seismic data, which themselves are expected to be quite different. This is because body wave travel times are inherently less sensitive to the depth of the crust-mantle boundary, as their long-distance propagation depends on integrated properties along the ray paths. In contrast, receiver functions depend only on sub-receiver structure, providing more precise constraints on the interface depth. Therefore, we refine global crustal thickness models to better represent observational uncertainties at each Apollo station by incorporating updated crustal thickness estimates from this study.

We carry out gravimetric inversions similar to those applied in recent studies of lunar and Martian crustal thickness (Kim et al., 2023; Wieczorek et al., 2013; Wieczorek et al., 2022), but explicitly incorporate the seismic uncertainties derived from our analysis above. We used the GRGM1200B_RM1_1E0 GRAIL gravity model of Goossens et al. (2020). All gravity computations were performed using a finite-amplitude technique to order 15 (Wieczorek & Phillips, 1998) (Supporting Information S1). We also increase the number of seismic tie-points across three scenarios to accommodate relative quality of seismic data analysis (Apollo 12; Apollo 12 and 16; and Apollo 12, 15, and 16). For an assumed average crustal thickness, we use GRAIL observations to infer crustal thickness variations for a range of permissible crustal porosities (6%–12%) and mantle densities (3,200–3,400 kg/m^3). We then calculate the χ^2 misfit between observed and predicted thicknesses at the tie-points for each assumed global average crustal thickness (see text in Supporting Information S1 for details). As in the study of Wieczorek et al. (2022) for Mars, we find that our crustal thickness models vary as a function of the density contrast between the crust and mantle, but are otherwise independent of the values used for the crustal and mantle density (Figure S22 in Supporting Information S1). We also find that the average crustal thickness of our final results depend strongly on the density contrast between the crust and mantle (Figures 3d–3f). On the other hand, the number of tie-point measurements has minimal impact on the final estimates, with each tie-point yielding consistent results, which reinforces the robustness of our method despite the limited distribution of Apollo landing sites on the lunar nearside. Across all tie-point scenarios considered, we find a consistent global average crustal thickness ranging from 29 to 47 km (1-σ). These estimates are slightly lower than but compatible with average crustal thicknesses that were assumed to create the two GRAIL crustal thickness maps of Wieczorek et al. (2013). The somewhat larger uncertainties in our results reflect the explicit inclusion of seismic uncertainties, which were not considered in the original GRAIL analysis.

Our polarization analysis approach is particularly well-suited to the analysis of modern digital seismograms that will be recorded by future lunar missions carrying advanced broadband instrumentation. Our model predicts crustal thicknesses of 22–28 km (PKT), 33–41 km (Schickard), 3–11 km (Crisium), and 48–61 km (Korolev) around the proposed landing sites of the Lunar Geophysical Network (LGN; See Haviland et al. (2022) for more details about these landing sites) (Figures 3g and 3h; Table S3 in Supporting Information S1). Notable upcoming missions include NASA's Farside Seismic Suite (FSS; Panning et al. (2022)), which will place a seismometer in the Schrödinger basin via the Commercial Lunar Payload Services initiative, and NASA's Artemis III mission, during which astronauts will deploy broadband seismometers near the lunar south pole as part of the Lunar Environment Monitoring Station (LEMS-A3; Schmerr et al. (2024)). Based on our models, we predict crustal thicknesses ranging from 8 to 15 km at the center of the Schrödinger basin, where the crust is thinnest, to 25–37 km at the basin's rim, near the expected landing site of the FSS. Across potential LEMS-A3 data acquisition sites, crustal thicknesses are estimated to vary more broadly, ranging from 30 to 60 km. These predictions for the south polar regions provide a benchmark for future measurements and hold significant implications for understanding the Moon's thermal evolution and interior structure.

Data Availability Statement

The Apollo seismic data is available via the International Federation of Digital Seismograph Networks (Nunn, 1969). The original data were collected from 1969 to 1977 (Latham et al., 1970) and have been imported to modern formats (Nunn et al., 2022). All results presented in Figure 3 and Figure S22, and Table S3 in Supporting Information S1 can be reproduced using the python-based open-source software ctplanet (Wieczorek, 2024). Gridded data sets for all crustal thickness models are available at Kim et al. (2025).

Acknowledgments
D.K. thanks Dr. Renee C. Weber at NASA's Marshall Space Flight Center for providing the lunar event master catalog used in this study. Authors also thank editor Daoyuan Sun and two anonymous reviewers whose constructive feedback greatly improved the manuscript. V.L. and N.C.S. acknowledge support from the NASA Solar System Exploration Research Virtual Institute GEODES (SSERVI Grant 80NSSC19M0216). The work of M.P.P was carried out at the Jet Propulsion Laboratory, California Institute of Technology, under a contract with the National Aeronautics and Space Administration (80NM0018D0004).

References

Binder, A. B. (1998). Lunar prospector: Overview. Science (Vol. *281*, (5382), pp. 1475–1476).

Blanchette-Guertin, J.-F., Johnson, C., & Lawrence, J. (2015). Effects of lateral variations in megaregolith thickness on predicted lunar seismic signals. *Geophysical Research Letters*, *42*(23), 10–171. https://doi.org/10.1002/2015gl066151

Bulow, R., Johnson, C., Bills, B., & Shearer, P. (2007). Temporal and spatial properties of some deep moonquake clusters. *Journal of Geophysical Research*, *112*(E9), E09003. https://doi.org/10.1029/2006je002847

Bulow, R., Johnson, C., & Shearer, P. (2005). New events discovered in the apollo lunar seismic data. *Journal of Geophysical Research*, *110*(E10), E10003. https://doi.org/10.1029/2005je002414

Burdick, L. J., & Langston, C. A. (1977). Modeling crustal structure through the use of converted phases in teleseismic body-wave forms. *Bulletin of the Seismological Society of America*, *67*(3), 677–691. https://doi.org/10.1785/bssa0670030677

Chenet, H., Lognonné, P., Wieczorek, M., & Mizutani, H. (2006). Lateral variations of lunar crustal thickness from the apollo seismic data set. *Earth and Planetary Science Letters*, *243*(1–2), 1–14. https://doi.org/10.1016/j.epsl.2005.12.017

Chung, D. H. (1973). Elastic wave velocities in anorthosite and anorthositic gabbros from apollo 15 and 16 landing sites. *Proceedings of the lunar science conference*, *4*, 2591.
Dainty, A. M., Toksöz, M. N., Anderson, K. R., Pines, P. J., Nakamura, Y., & Latham, G. (1974). Seismic scattering and shallow structure of the moon in oceanus procellarum. *The Moon*, *9*(1–2), 11–29. https://doi.org/10.1007/bf00565388
Drilleau, M., Beucler, É., Mocquet, A., Verhoeven, O., Moebs, G., Burgos, G., et al. (2013). A bayesian approach to infer radial models of temperature and anisotropy in the transition zone from surface wave dispersion curves. *Geophysical Journal International*, *195*(2), 1165–1183. https://doi.org/10.1093/gji/ggt284
Flinn, E. (1965). Signal analysis using rectilinearity and direction of particle motion. *Proceedings of the IEEE*, *53*(12), 1874–1876. https://doi.org/10.1109/proc.1965.4462
Garcia, R. F., Gagnepain-Beyneix, J., Chevrot, S., & Lognonné, P. (2011). Very preliminary reference moon model. *Physics of the Earth and Planetary Interiors*, *188*(1–2), 96–113. https://doi.org/10.1016/j.pepi.2011.06.015
Garcia, R. F., Khan, A., Drilleau, M., Margerin, L., Kawamura, T., Sun, D., et al. (2019). Lunar seismology: An update on interior structure models. *Space Science Reviews*, *215*(8), 1–47. https://doi.org/10.1007/s11214-019-0613-y
Gillet, K., Margerin, L., Calvet, M., & Monnereau, M. (2017). Scattering attenuation profile of the moon: Implications for shallow moonquakes and the structure of the megaregolith. *Physics of the Earth and Planetary Interiors*, *262*, 28–40. https://doi.org/10.1016/j.pepi.2016.11.001
Goins, N. R., Dainty, A. M., & Toksöz, M. N. (1981). Structure of the lunar crust at highland site apollo station 16. *Geophysical Research Letters*, *8*(1), 29–32. https://doi.org/10.1029/gl008i001p00029
Goodling, P. J., Lekic, V., & Prestegaard, K. (2018). Seismic signature of turbulence during the 2017 oroville dam spillway erosion crisis. *Earth Surface Dynamics*, *6*(2), 351–367. https://doi.org/10.5194/esurf-6-351-2018
Goossens, S., Sabaka, T., Wieczorek, M., Neumann, G., Mazarico, E., Lemoine, F., et al. (2020). High-resolution gravity field models from grail data and implications for models of the density structure of the moon's crust. *Journal of Geophysical Research: Planets*, *125*(2), e2019JE006086. https://doi.org/10.1029/2019je006086
Haviland, H. F., Weber, R. C., Neal, C. R., Lognonné, P., Garcia, R. F., Schmerr, N., et al. (2022). The lunar geophysical network landing sites science rationale. *The Planetary Science Journal*, *3*(2), 40. https://doi.org/10.3847/psj/ac0f82
Irving, J. C., Lekić, V., Durán, C., Drilleau, M., Kim, D., Rivoldini, A., et al. (2023). First observations of core-transiting seismic phases on mars. *Proceedings of the National Academy of Sciences*, *120*(18), e2217090120. https://doi.org/10.1073/pnas.2217090120
Jolliff, B. L., Gillis, J. J., Haskin, L. A., Korotev, R. L., & Wieczorek, M. A. (2000). Major lunar crustal terranes: Surface expressions and crust-mantle origins. *Journal of Geophysical Research*, *105*(E2), 4197–4216. https://doi.org/10.1029/1999je001103
Khan, A., Connolly, J. A., Pommier, A., & Noir, J. (2014). Geophysical evidence for melt in the deep lunar interior and implications for lunar evolution. *Journal of Geophysical Research: Planets*, *119*(10), 2197–2221. https://doi.org/10.1002/2014je004661
Khan, A., & Mosegaard, K. (2002). An inquiry into the lunar interior: A nonlinear inversion of the apollo lunar seismic data. *Journal of Geophysical Research*, *107*(E6), 3-1. https://doi.org/10.1029/2001je001658
Khan, A., Pommier, A., Neumann, G., & Mosegaard, K. (2013). The lunar moho and the internal structure of the moon: A geophysical perspective. *Tectonophysics*, *609*, 331–352. https://doi.org/10.1016/j.tecto.2013.02.024
Kim, D., Banerdt, W. B., Ceylan, S., Giardini, D., Lekić, V., Lognonné, P., et al. (2022). Surface waves and crustal structure on mars. *Science*, *378*(6618), 417–421. https://doi.org/10.1126/science.abq7157
Kim, D., Duran, C., Giardini, D., Plesa, A.-C., Stähler, S. C., Boehm, C., et al. (2023). Global crustal thickness revealed by surface waves orbiting mars. *Geophysical Research Letters*, *50*(12), e2023GL103482. https://doi.org/10.1029/2023gl103482
Kim, D., Lekić, V., Irving, J. C., Schmerr, N., Knapmeyer-Endrun, B., Joshi, R., et al. (2021). Improving constraints on planetary interiors with pps receiver functions. *Journal of Geophysical Research: Planets*, *126*(11), e2021JE006983. https://doi.org/10.1029/2021je006983
Kim, D., Lekic, V., Wieczorek, M., Schmerr, N., Gollins, G., & Panning, M. (2025). New lunar crustal thickness models [dataset]. *Zenodo*. https://doi.org/10.5281/zenodo.15632211
Kivelson, M., Khurana, K., Means, J., Russell, C., & Snare, R. (1992). The galileo magnetic field investigation. *Space Science Reviews*, *60*, 357–383. https://doi.org/10.1007/978-94-011-2512-3_15
Knapmeyer-Endrun, B., Panning, M. P., Bissig, F., Joshi, R., Khan, A., Kim, D., et al. (2021). Thickness and structure of the martian crust from insight seismic data. *Science*, *373*(6553), 438–443. https://doi.org/10.1126/science.abf8966
Koper, K. D., & Hawley, V. L. (2010). Frequency dependent polarization analysis of ambient seismic noise recorded at a broadband seismometer in the central United States. *Earthquake Science*, *23*(5), 439–447. https://doi.org/10.1007/s11589-010-0743-5
Korn, M. (1993). Determination of site-dependent scattering q from p-wave coda analysis with an energy-flux model. *Geophysical Journal International*, *113*(1), 54–72. https://doi.org/10.1111/j.1365-246x.1993.tb02528.x
Lammlein, D. R., Latham, G. V., Dorman, J., Nakamura, Y., & Ewing, M. (1974). Lunar seismicity, structure, and tectonics. *Reviews of Geophysics*, *12*(1), 1–21. https://doi.org/10.1002/9781118782118.ch1
Latham, G. V., Ewing, M., Press, F., Sutton, G., Dorman, J., Nakamura, Y., et al. (1970). Passive seismic experiment. *Science*, *167*(3918), 455–457. https://doi.org/10.1126/science.167.3918.455
Lognonné, P., Gagnepain-Beyneix, J., & Chenet, H. (2003). A new seismic model of the moon: Implications for structure, thermal evolution and formation of the moon. *Earth and Planetary Science Letters*, *211*(1–2), 27–44. https://doi.org/10.1016/s0012-821x(03)00172-9
Mark, N., & Sutton, G. (1975). Lunar shear velocity structure at apollo sites 12, 14, and 15. *Journal of Geophysical Research*, *80*(35), 4932–4938. https://doi.org/10.1029/jb080i035p04932
Miljković, K., Wieczorek, M. A., Collins, G. S., Solomon, S. C., Smith, D. E., & Zuber, M. T. (2015). Excavation of the lunar mantle by basin-forming impact events on the moon. *Earth and Planetary Science Letters*, *409*, 243–251. https://doi.org/10.1016/j.epsl.2014.10.041
Moriarty, D. P., Dygert, N., Valencia, S. N., Watkins, R. N., & Petro, N. E. (2021). The search for lunar mantle rocks exposed on the surface of the moon. *Nature Communications*, *12*(1), 4659. https://doi.org/10.1038/s41467-021-24626-3
Nakamura, Y., Latham, G. V., & Dorman, H. J. (1982). Apollo lunar seismic experiment—Final summary. *Journal of Geophysical Research*, *87*(S01), A117–A123. https://doi.org/10.1029/jb087is01p0a117
Neumann, G. A., Zuber, M. T., Wieczorek, M. A., Head, J. W., Baker, D. M., Solomon, S. C., et al. (2015). Lunar impact basins revealed by gravity recovery and interior laboratory measurements. *Science Advances*, *1*(9), e1500852. https://doi.org/10.1126/sciadv.1500852
Nozette, S., Rustan, P., Pleasance, L., Kordas, J., Lewis, I., Park, H., et al. (1994). The clementine mission to the moon: Scientific overview. *Science*, *266*(5192), 1835–1839. https://doi.org/10.1126/science.266.5192.1835
Nunn, C. (1969). Apollo passive seismic experiments [dataset]. *International Federation of Digital Seismograph Networks*. https://doi.org/10.7914/SN/XA_1969
Nunn, C., Garcia, R. F., Nakamura, Y., Marusiak, A. G., Kawamura, T., Sun, D., et al. (2020). Lunar seismology: A data and instrumentation review. *Space Science Reviews*, *216*(5), 89. https://doi.org/10.1007/s11214-020-00709-3

Nunn, C., Nakamura, Y., Kedar, S., & Panning, M. P. (2022). A new archive of apollo's lunar seismic data. *The Planetary Science Journal*, *3*(9), 219. https://doi.org/10.3847/psj/ac87af

Onodera, K., Kawamura, T., Tanaka, S., Ishihara, Y., & Maeda, T. (2022). Quantitative evaluation of the lunar seismic scattering and comparison between the earth, mars, and the moon. *Journal of Geophysical Research: Planets*, *127*(12), e2022JE007558. https://doi.org/10.1029/2022je007558

Paige, D. A., Siegler, M. A., Zhang, J. A., Hayne, P. O., Foote, E. J., Bennett, K. A., et al. (2010). Diviner lunar radiometer observations of cold traps in the moon's south polar region. *science*, *330*(6003), 479–482. https://doi.org/10.1126/science.1187726

Panning, M., Kedar, S., Bowles, N., Bugby, D., Calcutt, S., Cutler, J., et al. (2022). Farside seismic suite (fss): Surviving the lunar night and delivering the first seismic data from the farside of the moon. *53rd lunar and planetary science conference*, *2678*, 1576.

Park, J., VernonIII, F. L., & Lindberg, C. R. (1987). Frequency dependent polarization analysis of high-frequency seismograms. *Journal of Geophysical Research*, *92*(B12), 12664–12674. https://doi.org/10.1029/jb092ib12p12664

Saito, T., Sato, H., & Ohtake, M. (2002). Envelope broadening of spherically outgoing waves in three-dimensional random media having power law spectra. *Journal of Geophysical Research*, *107*(B5), ESE–3. https://doi.org/10.1029/2001jb000264

Samson, J. (1983). Pure states, polarized waves, and principal components in the spectra of multiple, geophysical time-series. *Geophysical Journal International*, *72*(3), 647–664. https://doi.org/10.1111/j.1365-246x.1983.tb02825.x

Schmerr, N. C., Benna, M., McCall, N., Bailey, S., DellaGiustina, D., Bray, V., et al. (2024). The lunar environmental monitoring station: An artemis 3 deployed instrument. *LPI Contribution*, *3060*, 6010.

Shi, J., Wang, T., Chen, H., Yang, M., Chen, L., Hui, H., et al. (2023). Differences in scattering properties of the shallow crusts of earth, mars, and the moon revealed by p-wave receiver functions. *Journal of Geophysical Research: Planets*, *128*(8), e2022JE007676. https://doi.org/10.1029/2022je007676

Smith, D. E., Zuber, M. T., Neumann, G. A., Lemoine, F. G., Mazarico, E., Torrence, M. H., et al. (2010). Initial observations from the lunar orbiter laser altimeter (lola). *Geophysical Research Letters*, *37*(18). https://doi.org/10.1029/2010gl043751

Stähler, S. C., Khan, A., Banerdt, W. B., Lognonné, P., Giardini, D., Ceylan, S., et al. (2021). Seismic detection of the martian core. *Science*, *373*(6553), 443–448. https://doi.org/10.1126/science.abi7730

Stockwell, R. G., Mansinha, L., & Lowe, R. (1996). Localization of the complex spectrum: The s transform. *IEEE Transactions on Signal Processing*, *44*(4), 998–1001. https://doi.org/10.1109/78.492555

Taylor, G. J., & Wieczorek, M. A. (2014). Lunar bulk chemical composition: A post-gravity recovery and interior laboratory reassessment. *Philosophical Transactions of the Royal Society A: Mathematical, Physical and Engineering Sciences*, *372*(2024), 20130242. https://doi.org/10.1098/rsta.2013.0242

Toksöz, M. N., Dainty, A. M., Solomon, S. C., & Anderson, K. R. (1974). Structure of the moon. *Reviews of Geophysics*, *12*(4), 539–567. https://doi.org/10.1029/rg012i004p00539

Vinnik, L., Chenet, H., Gagnepain-Beyneix, J., & Lognonne, P. (2001). First seismic receiver functions on the moon. *Geophysical Research Letters*, *28*(15), 3031–3034. https://doi.org/10.1029/2001gl012859

Wahl, D., Wieczorek, M., Wünnemann, K., & Oberst, J. (2020). Crustal porosity of lunar impact basins. *Journal of Geophysical Research: Planets*, *125*(4), e2019JE006335. https://doi.org/10.1029/2019je006335

Weber, R. C., Lin, P.-Y., Garnero, E. J., Williams, Q., & Lognonné, P. (2011). Seismic detection of the lunar core. *science*, *331*(6015), 309–312. https://doi.org/10.1126/science.1199375

Wieczorek, M. A. (2024). ctplanet: Version 0.2.10 [software]. *Zenodo*. https://doi.org/10.5281/zenodo.14572797

Wieczorek, M. A., Broquet, A., McLennan, S. M., Rivoldini, A., Golombek, M., Antonangeli, D., et al. (2022). Insight constraints on the global character of the Martian crust. *Journal of Geophysical Research: Planets*, *127*(5), e2022JE007298. https://doi.org/10.1029/2022je007298

Wieczorek, M. A., Jolliff, B. L., Khan, A., Pritchard, M. E., Weiss, B. P., Williams, J. G., & others (2006). The constitution and structure of the lunar interior. *Reviews in Mineralogy and Geochemistry*, *60*(1), 221–364. https://doi.org/10.2138/rmg.2006.60.3

Wieczorek, M. A., Neumann, G. A., Nimmo, F., Kiefer, W. S., Taylor, G. J., Melosh, H. J., et al. (2013). The crust of the moon as seen by grail. *Science*, *339*(6120), 671–675. https://doi.org/10.1126/science.1231530

Zhu, L., & Kanamori, H. (2000). Moho depth variation in southern California from teleseismic receiver functions. *Journal of Geophysical Research*, *105*(B2), 2969–2980. https://doi.org/10.1029/1999jb900322

Zuber, M. T., Smith, D. E., Lehman, D. H., Hoffman, T. L., Asmar, S. W., & Watkins, M. M. (2014). Gravity recovery and interior laboratory (grail): Mapping the lunar interior from crust to core. *GRAIL: Mapping the Moon's interior*, 3–24. https://doi.org/10.1007/978-1-4614-9584-0_2

References From the Supporting Information

Fuchs, K., & Müller, G. (1971). Computation of synthetic seismograms with the reflectivity method and comparison with observations. *Geophysical Journal International*, *23*(4), 417–433. https://doi.org/10.1111/j.1365-246x.1971.tb01834.x

Liu, Y., Wu, C., Xu, T., Zhao, L., & Teng, J. (2025). Fdfk2d: Efficient two-dimensional teleseismic wavefield modeling for receiver function analysis using a hybrid method. *Seismological Research Letters*, *96*(2A), 1163–1180. https://doi.org/10.1785/0220240231

Muller, G. (1985). The reflectivity method: A tutorial. *Journal of Geophysics*, *58*(1), 153–174.

Neumann, G. A. (2024). LOLA MOON_PA gridded dataset [Dataset]. *NASA Goddard Space Flight Center Planetary Geodesy Data Archive*. https://doi.org/10.60903/LOLA_PA

Petersson, N. A., & Sjogreen, B. (2010). *Reference guide to wpp version 2.0 (Tech. Rep.)*. Lawrence Livermore National Lab.(LLNL).

Petersson, N. A., & Sjögreen, B. (2018). High order accurate finite difference modeling of seismo-acoustic wave propagation in a moving atmosphere and a heterogeneous earth model coupled across a realistic topography. *Journal of Scientific Computing*, *74*(1), 290–323. https://doi.org/10.1007/s10915-017-0434-7

Smith, D. E., Zuber, M. T., Jackson, G. B., Cavanaugh, J. F., Neumann, G. A., Riris, H., et al. (2010). The lunar orbiter laser altimeter investigation on the lunar reconnaissance orbiter mission. *Space Science Reviews*, *150*(1–4), 209–241. https://doi.org/10.1007/s11214-009-9512-y

Wieczorek, M. A., & Meschede, M. (2018). Shtools: Tools for working with spherical harmonics. *Geochemistry, Geophysics, Geosystems*, *19*(8), 2574–2592. https://doi.org/10.1029/2018gc007529

Wieczorek, M. A., & Phillips, R. J. (1998). Potential anomalies on a sphere: Applications to the thickness of the lunar crust. *Journal of Geophysical Research*, *103*(E1), 1715–1724. https://doi.org/10.1029/97je03136